Thermally activated dependence of fatigue behaviour of CrMnFeCoNi high entropy alloy fabricated by laser powder-bed fusion

Minsoo Jin[1,*], Ehsan Hosseini[2], Stuart. R. Holdsworth[2], Minh-Son Pham[1,*]

1. Department of Materials, Imperial College London, Exhibition Road, South Kensington, London SW7 2AZ, UK
2. EMPA, Swiss Federal Laboratories for Materials Science and Technology, Überlandstrasse 129, 8600 Dübendorf, Switzerland
* Corresponding authors: min.jin12@imperial.ac.uk and son.pham@imperial.ac.uk

Keywords: High-entropy alloys, Additive manufacturing, Laser powder bed fusion, Themal fatigue, Cyclic plasticity

Abstract

The CrMnFeCoNi high-entropy alloy demonstrates a promising potential for applications over a range of temperature. The alloy also shows excellent printability to be fabricated by additive manufacturing for complex structures. Nevertheless, there are limited studies on the thermo-mechanical behaviour of the alloy, in particular when fabricated by laser powder-bed fusion. This study provides an in-depth understanding of the relationship between as-built cellular microstructures and fatigue behaviour at a range of temperatures (22-600 °C). The alloy exhibits a very short duration cyclic hardening with a low hardening rate followed by a cyclic softening. The high density of dislocations already existing in as-built condition were able to accommodate most of the prescribed strain. Hence, only a small number of mobile dislocations needs to be generated, causing a short cyclic hardening phase. Upon further loading, the back stress associated with the long-range stress field was dominant factor governing the cyclic softening behaviour. The similitude relationship provided insights into the stability of as-built cells, in particular it explains why as-built cells did not evolve during cyclic loading at 22 °C. The significant reduction in dislocation density due to the increased annihilation rate and untanglement of dislocation substructures at elevated temperatures led to a decrease in cyclic strength and related properties (yield stress, friction and back stress, hysteresis loop shape parameter and energy per cycle). The LPBF HEA shows an insignificant strain rate dependence of the primary cyclic hardening and softening in the range of 10^{-3} s^{-1} and 10^{-2} s^{-1}. However, the dynamic strain ageing results in a secondary cyclic hardening at 400 °C and the reversed strain sensitivity at temperatures from 200 to 400 °C. The fracture mode was transgranular at 22-400 °C but changed to more intergranular-like at 600 °C due to the decohesion of grain boundaries, resulting in a reduction in fatigue life.

1. Introduction

Additive manufacturing (AM) has increasingly been used to fabricate alloys in recent decades. The advantage of the AM process is that the layer-by-layer fabrication process can build alloy components into a desired complex shape with enhanced geometric optimisation. Commonly used alloys such as 316L stainless steel, nickel-based Inconel 718 and Ti6Al4V have been successfully fabricated by AM [1–8]. In comparison to conventional manufacturing, AM results in cellular (or dendritic) microstructures with dense dislocation tangles located at the cell boundaries due to inherently fast cooling rates of AM. Such microstructures were found to enhance the mechanical strength of alloys [9–15]. One of the main aims of ongoing research relating to AM fabrications is to produce structurally sound components of existing alloys while combining freedom of design and remarkable mechanical properties. However, most of all of the alloys used for AM were designed for other processes such as casting, partly contributing to the difficulty in fabricating structurally sound components out of these materials. The successful fabrication of components via AM strongly depends on the printability of their alloy [16]. An alloy with a good printability allows the fabrication with wider processing windows to form a dimensionally accurate component with a minimal density of cracks and porosity and desired mechanical properties. Therefore, there is an increasing need to search for printable alloys that are more suitable for AM.

Amongst the new types of alloys, high-entropy alloys (HEAs) hold great potential with some exhibiting excellent printability. HEAs consist of 5 or more principal elements in (near) equiatomic concentration, and these multicomponent alloys were first introduced by Cantor *et al.* [17] and Yeh *et al.* [18]. The name "high entropy" denotes the high configurational entropy of mixing, which is significantly larger than that of conventional alloys [18–20]. Therefore, there has been an increasing number of studies focusing on fabricating HEA components by AM processes [21–25]. Moreover, HEAs have received significant attention in the materials community thanks to their outstanding mechanical properties and promising fatigue and corrosion resistance [19,20,26–34]. The equiatomic CrMnFeCoNi is the most studied HEA fabricated by AM. The main reason for the great interest in this HEA is its excellent printability [13,14,35–37]. The alloy has a relatively low solidification gradient (i.e. the gradient of solid fraction during solidification against temperature curve) at the terminal stage in comparison to that of 316L and a narrow freezing range (170 K) which suggest a low susceptibility to solidification/liquation cracking during the AM process [14,15]. In addition, CrMnFeCoNi HEAs exhibit an excellent mechanical behaviour under monotonic loading over a wide range of temperatures including cryogenic conditions [30,33,34,38]. Moreover, the HEA's resistance to fatigue crack propagation is comparable to austenitic steels and TWIP steels at room temperature (20 °C) and -75 °C [39,40]. In particular, the fatigue life behaviour at room and elevated temperatures (e.g. at 550 °C) was reported to be comparable to austenitic FCC steels [41,42]. These results indicate this alloy holds potential as a reliable structural alloy not only at cryogenic conditions but also at elevated temperatures In particular, additive manufacturing is considered as a feasible method that enables to build infrastructures, fabricate spacecraft components and supplies for critical maintenances in the circumstances of interplanetary explorations where the availability of cargo resupply is extremely limited. The excellent mechanical properties and fatigue performances of the CrMnFeCoNi HEA over a range of temperatures makes it particularly a suitable material for aerospace and space applications.

Laser Powder-Bed Fusion (LPBF) is currently the most effective AM technique in manufacturing intrincate components. The fabrication of this HEA by LPBF can offer enhanced performance at high temperatures over the cast (or wrought) alloy thanks to the unique microstructure generated in LPBF. For example, Lin et al.'s study [43] showed the dense dislocation networks in the FeCoCrNi HEA (subset of the CrMnFeCoNi HEA) fabricated by LPBF increased the storage rate of

deformation energy significantly during deformation. Kim *et al.*'s study [44] demonstrates that the AM alloy can have excellent compressive properties at elevated temperatures in the range from 500-700 °C [44]. At those temperatures the compressive yield strength exceeds 540 MPa, which is more than double that of the conventionally manufactured HEAs at room temperature (~250 MPa) [45], suggesting that the combination of LPBF and CrMnFeCoNi offers potential for elevated temperature applications.

Most of mechanical systems and structures operate under cyclic loadings over a range of temperatures, and cyclic plasticity and fatigue behaviour are found to be responsible for most of catastrophic failures [46–48]. The cyclic plasticity and fatigue damage is closely related to microstructures [46–53]. Thus, if we wish to use this HEA fabricated by LPBF (and by AM in general) for structural applications, it is necessary to understand the evolution of solidification microstructures at room and elevated temperatures and the consequent influence on cylic plasticity and fatigue. Currently, there are only a few studies concerning the cyclic plasticity and fatigue damage at room temperature in relation to the solidification microstructure of this alloy fabricated by LPBF [15,54]. To the authors' knowledge, while there are many studies on the fatigue and monotonic performances of the alloy (either in the cast, wrought or AM condition) at cryogenic and room temperature [15,39–41,55,56], only a limited number of studies have been performed on high temperatures [42]. Most importantly, there were no previous studies on the cyclic plasticity and fatigue behaviour at elevated temperatures and strain rates of this alloy fabricated by LPBF (and more broadly AM). Therefore, this study aims to provide an in-depth understanding of the relationship between the microstructure in the LPBF CrMnFeCoNi and fatigue behaviour over a range of temperatures (22-600 °C) and at two different strain rates (10^{-3} s^{-1} and 10^{-2} s^{-1}). The characteristics of cyclic deformation such as maximum cyclic stress, friction stress, back stress, the stress-strain loop shape parameter [57–59], and cyclic hardening and softening behaviour were measured and analysed to understand the thermally activated dependence of cyclic plasticity. In particular, friction stress and back stress were examined in detail to study the short- and long-range interactions between dislocations during cyclic loading [49,59,60]. The evolution of friction and back stresses provides insights into the microstructure evolution during cyclic loading. Furthermore, in the absence of dislocation cells before the loading (i.e. well-annealed conditions), dislocation substructure evolves from randomly distributed to tangled then finally to dislocation cellular structures in response to cyclic loading [49,58–64]. Dislocation cells formed in cyclic loading are found to be influential in the strength and constitutive behaviour [49,60–64]. In the case of AM alloys, solidification microstructure with dislocation cells is predominantly present in the as-fabricated condition already before the mechanical loading. Hence, in this study, dislocation cells already present in the as-built condition were characterized in detail before and after the fatigue tests at 22-600 °C to understand their roles and their stability during cyclic deformation. This study, in particular, focuses on relating the dislocation cells to the cyclic stress response using the similitude relationship [61,62,64–66].

2. Methods

2.1 Materials and laser powder-bed fusion

The pre-alloyed CrMnFeCoNi powders for the current study were provided by H.C. Starck Surface Technology & Ceramic Powders GmbH. Table 1 shows the nominal chemical compositions of the powders. The average size of powder particles is about 7.5 μm, and the particle size varies from 3 to 45 um (Figure 1). Fatigue specimens were printed on a 316L stainless steel substrate (without pre-heating) in the argon atmosphere with a purity level of 99.998% (argon gas was provided by BOC) by using a Renishaw AM250 printer equipped with a modulated wave fibre laser. The selected print parameters were a laser power of 200W, a hatch spacing of 85 μm, an exposure time of 80 μs, a point distance of 60 μm, a layer height of 50 μm and a spot size of 65 μm. These parameters were optimized for the 316L stainless steel [10], which is also of the same FeCrNi alloy system as the CrMnFeCoNi, and also used to manufacture the CrMnFeCoNi samples previously [14,15]. The chessboard scanning pattern with 67° rotation between each layer was employed to print cylindrical dog-bone fatigue samples with a gauge length of 18 mm and a diameter of 4 mm (Figure 2). The build direction of dog-bone samples was parallel to their longitudinal axis. The surfaces of printed samples were machined to a surface roughness of 0.2 Ra in order to eliminate the presence of sub-surface defects (e.g., key-hole pores).

Table 1. Nominal chemical composition of the HEA powder

Element	Cr	Mn	Fe	Co	Ni
wt.%	18.2	17.9	19.5	Balance	21.2

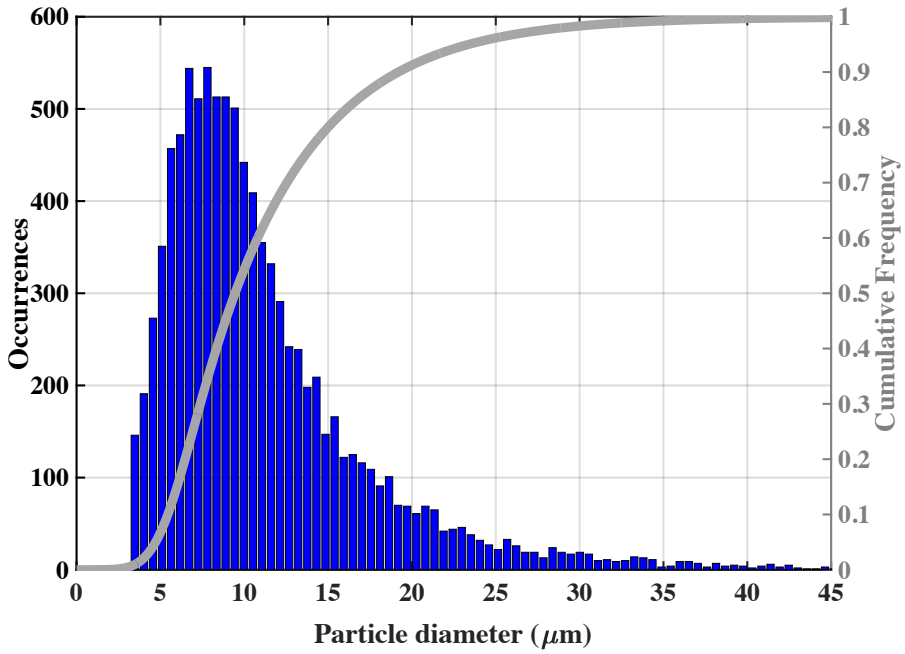


Figure 1. The CrMnFeCoNi powder particle size distribution (blue bar charts, y-axis on the left-hand side) and cumulative distribution of the particle size (grey line, y-axis on the right-hand side)

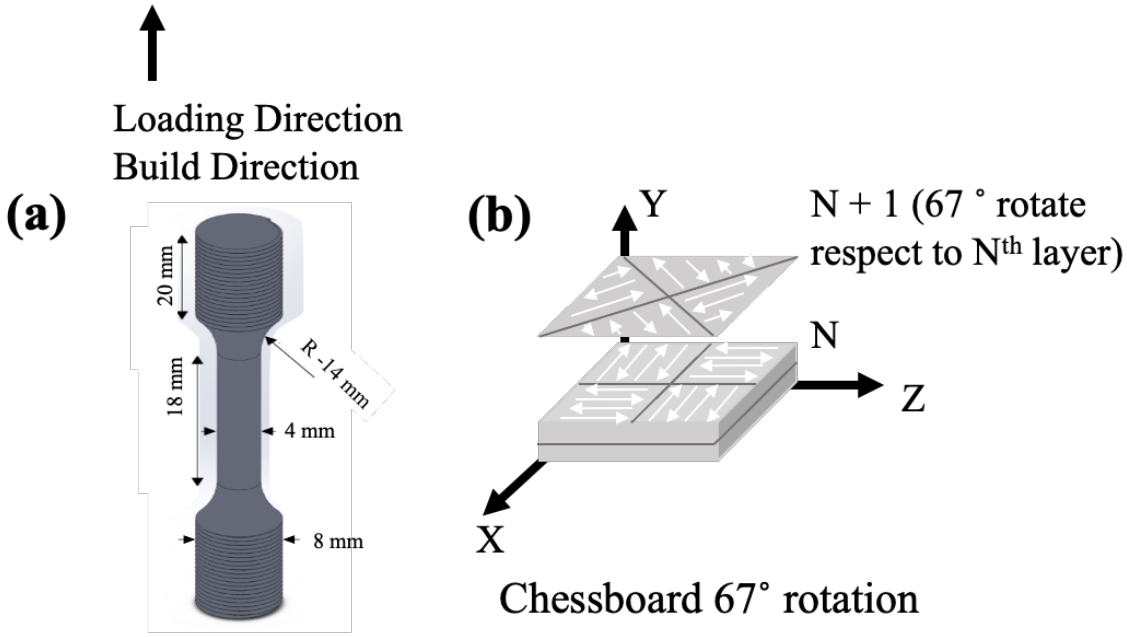


Figure 2. Schematics showing (a) the cylindrical dog-bone specimens and (b) chessboard scanning strategy pattern - each layer was subdivided into 4x4mm islands whose scan directions were 90° to those in the neighbouring islands and there was a rotation of 67° between subsequent layers.

2.2 *Microstructure characterisation*

Fractography of the fatigued samples were performed using a Zeiss™ Auriga scanning electron microscope (SEM). The fatigued samples were cut along their longitudinal axis (that was parallel to both the loading and build direction) for microstructure analyses. After cutting, samples were ground using 1200, 2400, and 4000 grit SiC papers in sequence then polished in an OP-S solution with 0.4 μm colloidal silica particles for electron backscattered diffraction (EBSD) analyses. EBSD analyses were carried out using a Zeiss™ Sigma 300 SEM equipped with a Field Emission Gun (FEG) electron source and a voltage of 20 kV. EBSD analyses were set at a step size of 0.5 μm per pixel and grain boundaries were defined when a misorientation larger than 5° was detected. The MTEX toolbox [67] and the dislocation density estimation function by Pantleon [68] were employed to analyse geometrically necessary dislocation (GND) density. Taylor factors of the fatigued samples were calculated from the EBSD maps using the MTEX toolbox [67] that was developed from a study on Taylor theory of polycrystal plasticity by Bunge [69]. Discs with a diameter of 3 mm were prepared from the gauge parts of fatigue samples, then electrochemically polished at 20 V and -20 °C using a twin-jet Struers Tenupol and an electrolyte consisting of 10% perchloric acid in methanol for Transmission Electron Microscopy (TEM) investigation. Bright Field (BF) TEM was performed using a JEOL 2100F field emission TEM operating at 200 kV. BF TEM images were subsequently analysed using the Image J software [70] to measure the diameter of dislocation cells.

2.3 Mechanical testing and cyclic plasticity analysis

Fatigue tests were performed at a range of temperatures (22-600 °C) in ambient condition under strain control at ± 0.5 % strain amplitude (R=-1) with strain rates of 10^{-2} s^{-1} and 10^{-3} s^{-1}. MATLAB-based subroutines developed by Pham *et al.* [57–59] were used to extract material's cyclic loading responses such as: elastic modulus, elastic strain, plastic strain, yield stress, friction stress, back stress and maximum stress for every cycle. Fatigue life was defined at a number of cycles when maximum stress response dropped by 20 % from a plateau region as shown in Figure 3a. Cyclic softening and cyclic hardening rates were calculated from maximum stress curves with a fitting function of $\sigma_{max} = a\log(N)+b$, where N is the number of cycles, a is the hardening/softening rate, and b is a constant (Figure 3b). Furthermore, cyclic deformation behaviour was analysed by evaluating the loop shape parameter [57,71], which is the ratio between the stress-strain hysteresis loop area and the area of the rectangle constructed by drawing four straight lines parallel to strain and stress axes and going through maximum and minimum stresses of hysteresis loop (the rectangle with blue dash lines shown in Figure 3c). The area of stress-strain hysteresis loop represents energy absorbed in the samples per a cycle, which is the strain energy density per unit volume. The energy of every cycle was analysed to investigate damage evolution. The yield stress in cyclic loading (σ_y in Figure 3c) was evaluated at an offset strain of 0.01 %. Figure 3 below shows the evaluation of friction stress (σ_F) and back stress (σ_B) from cyclic hysteresis loop by using the method of Cottrell [60,72].

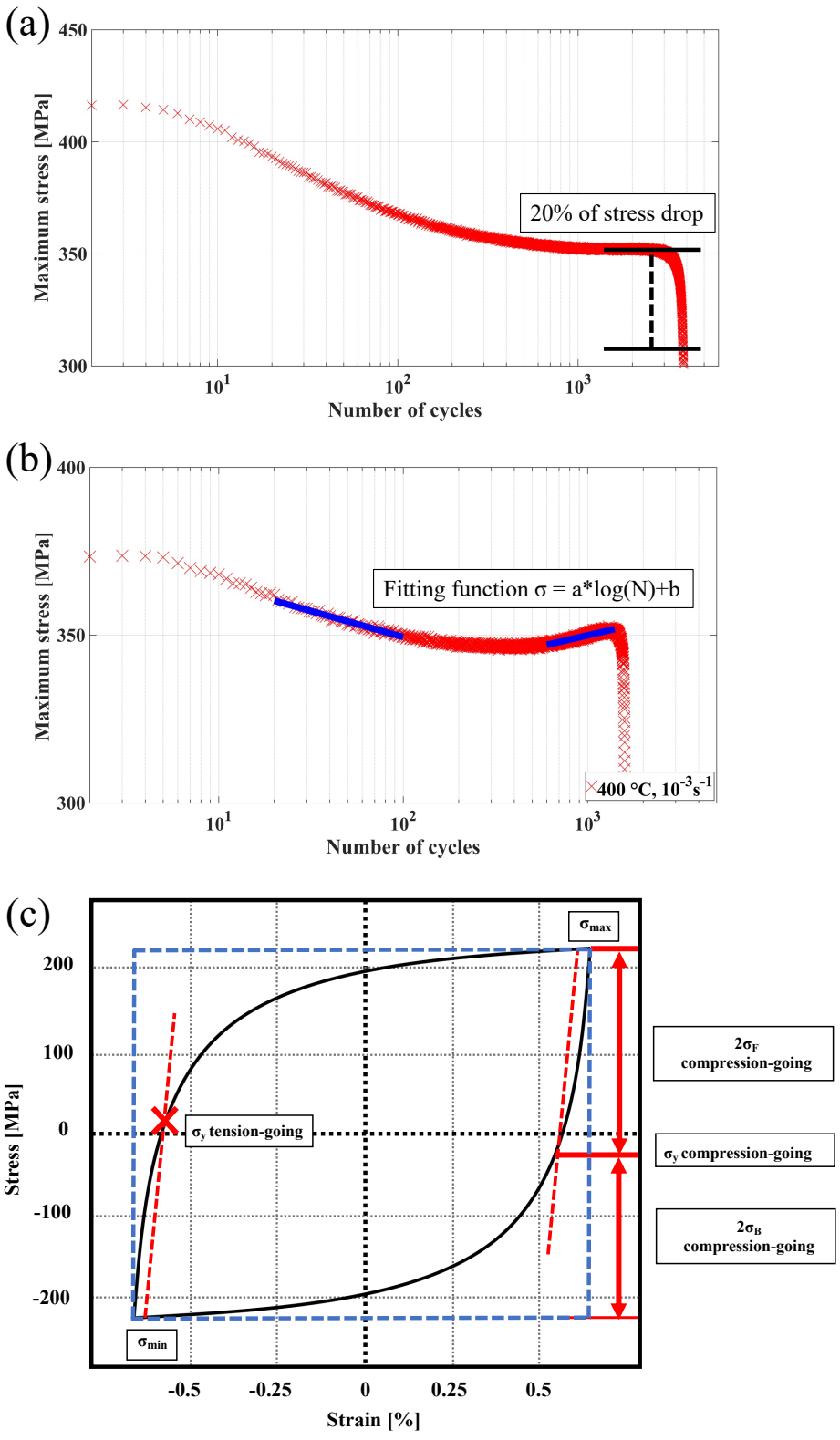


Figure 3. (a) Fatigue lives corresponding to 20% of maximum stress drop. (b) Representation of the fitting procedure to measure the rate of change of cyclic deformation response. (c) Schematic of quantitative measurement of friction stress (σ_F) and back stress (σ_B) from cyclic loading hysteresis loop, where both compression-going and tension-going σ_y is the offset yield stress evaluated at an offset strain of 0.01%

2.4 Similitude relations and cell diameter

The similitude relation equation (Equation 1) [61,62,64–66] and the relation between the macro-stress and critical resolved shear stress (Equation 2) [73] are rearranged to Equation 3 to calculate the diameter of cells that are supposed to form under cyclic loading should no dislocation cells be present before the cyclic loading:

$$\tau_{CRSS} = \frac{K\mu b}{d} \quad (1)$$

$$\sigma_y = M\tau_{CRSS} \quad (2)$$

$$d = \frac{MK\mu b}{\sigma_y} \quad (3)$$

where τ_{CRSS} is the critical resolved shear stress, K is the similitude coefficient, μ is the shear modulus, b is the magnitude of Burger's vector, d is the cell diameter, σ_y the yield stress, and M is the Taylor factor. The similitude coefficient K for FCC metals is found to be from 5 to 10 [64]. Therefore, as shown in Table 2, the similitude coefficient of 5 or 10 was used for the dislocation cell diameter calculation in this study. Table 2 also lists the values of other variables which were used for Equation 3 to estimate the cell diameter. The value of shear modulus of CrMnFeCoNi HEAs at 22, 200, 400 and 600 °C was obtained from Gludovatz *et al.* [74]. Lattice parameter is dependent on temperature which means that the magnitude of Burgers vector also changes with temperature. The lattice parameter of the CrMnFeCoNi HEA at an ambient temperature is reported to be 3.597 Å [75,76]. The lattice parameters at different elevated temperatures (200-600 °C) were calculated using the equation by Okada *et al.* [77] based on the measurement of thermal expansion coefficient of this HEA done by Laplanche *et al.* [76]. The values of calculated lattice parameters are 3.61 Å, 3.628 Å, and 3.646 Å at 200 °C, 400 °C and 600 °C, respectively (Table 2). For the similitude coefficient calculation, the instantaneous yield stress right before the loading, i.e. the maximum stress in relation to the start stress (i.e. minimum stress) of a loading transient (σ_{max} - σ_{min}) (Figure 3c) was used to calculate the size of dislocation cells according to Eqn. 2 and 3.

Table 2. The identification of parameters to calculate the size of dislocation cells

Temperature (°C)	Assumed Similitude coefficient, K	Calculated Taylor factor, M	Shear modulus, μ (GPa) [74]	Magnitude of Burgers vector, b (Å)	Instantenous yield stress, σ_y (MPa)
22	5 - 10	3.1	80 ± 2	2.54	830 ± 30
200	5 - 10	3.05	75 ± 2	2.55	700 ± 30
400	5 - 10	3.11	70 ± 2	2.57	680 ± 20
600	5 - 10	3.07	60 ± 2	2.58	620 ± 20

3. Results

3.1 Cyclic deformation behaviour

Table 3 shows fatigue lives, cyclic softening rate and rate of secondary cyclic hardening of all the tested conditions. In general, the CrMnFeCoNi HEA fabricated by LPBF exhibited slight cyclic hardening at the early stage of cyclic loading but only for a small number of cycles (about 5~10 cycles) (Figure 3a). Table 3 shows that the absolute rate of cyclic softening decreased with increasing the loading temperature for the two examined strain rates. In detail, the cyclic softening rate decreased from 46.1 at 22 °C to 17.0 at 400 °C at the strain rate of 10^{-3} s^{-1}. The cyclic softening rate at the higher strain rate (10^{-2} s^{-1}) also decreased from 37.1 to 23.2 as the temperature increased from 22 °C to 400 °C. Concerning the strain rate dependence, the cyclic softening rate was higher at the lower strain rate at 22 °C, suggesting that the cyclic softening happened more obviously at the lower strain rate. However, the cyclic softening rate at the lower strain rate increasingly became lower than that of the higher strain rate for temperatures above 200 °C. Most interestingly, the sample tested at 400 °C and 10^{-3} s^{-1} exhibited a significant secondary hardening with a rate of +12.8. Fatigue lives of the HEA were calculated as the number of cycles at the 20 % drop in maximum stress response (Table 3, last column). Fatigue life was seen to be most reduced at 600 °C consistently for the two strain rates.

Table 3. The rates of cyclic softening, secondary hardening and fatigue lives of the samples at 20 % maximum stress drop (Note: '-' indicates "not applicable")

Condition	Rate of cyclic softening (MPa/cycle)	Rate of secondary hardening (MPa/cycle)	$N_{20\%}$ (Cycles)
22 °C, ± 0.5 %, 10^{-3} s^{-1}	46.1	-	2630
200 °C, ± 0.5 %, 10^{-3} s^{-1}	35.8	-	3850
400 °C, ± 0.5 %, 10^{-3} s^{-1}	17.0	12.8	1590
600 °C, ± 0.5 %, 10^{-3} s^{-1}	-	-	80
22 °C, ± 0.5 %, 10^{-2} s^{-1}	37.1	-	1940
200 °C, ± 0.5 %, 10^{-2} s^{-1}	38.8	-	3210
400 °C, ± 0.5 %, 10^{-2} s^{-1}	23.2	-	2700
600 °C, ± 0.5 %, 10^{-2} s^{-1}	-	-	460

3.3 Microstructure evolution

Figure 4 show the estimates of geometrically necessary dislocation (GND) density of CrMnFeCoNi in the as-built condition (Fig. 3a) and after fatigue (Fig. 3b-e) based on the crystallographic kernel misorientation measured by EBSD mapping. In general, there was a higher GND density in the region within 75 µm from fracture surface at all test temperatures (Figure 4b-e). The dense GNDs near the fracture surface is a result of the high degree of plastic deformation induced by the crack tip microplasticity. The GND density in the region more than 75 µm away from fracture surface at 22 °C and 200 °C appears similar to the GND density in the as-built state (Figure 4a). Reduction in GNDs was observed after fatigue at temperatures above 200 °C (Figures 3d and e). The higher dislocation mobility at higher temperatures resulted in the faster recovery process, hence GND density was reduced. However, the GND density at 600 °C near the fracture surface appeared higher than that at 400 °C. This could be due to the much shorter duration of the fatigue test at 600 °C (only 80 cycles, Table 3). Although the dislocation mobility was higher, the number of cycles was too short for the annihilation and rearrangement of dislocations. Thereby, the smaller reduction in GNDs at 600 °C resulted in relatively higher GND density compared to at 400 °C.

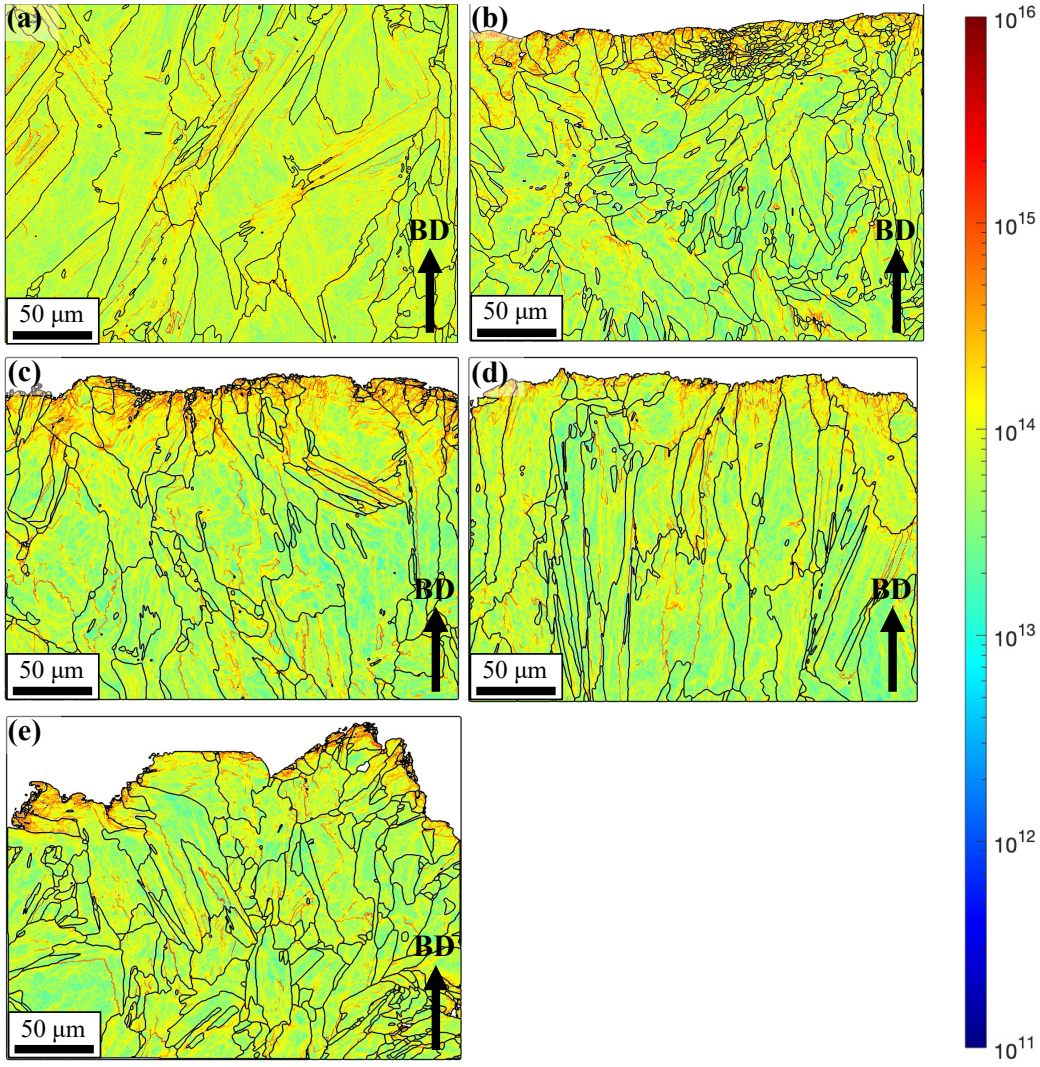


Figure 4. Estimated geometrically necessary dislocations (GND) density of CrMnFeCoNi HEA (a) in the as-built condition; and at the region near fracture surface after cyclic loading at the strain rate of 10^{-3} 1/s (b) at 22 °C, (c) at 200 °C, (d) at 400 °C and (e) at 600 °C.

The solidification microstructure with dense dislocations at boundaries was revealed by transmission electron microscopy. Figure 5a shows the solidification microstructure of LPBF CrMnFeCoNi consisted of solidification cells with a size ranging from 0.5 to 1 μm and dense dislocation tangles present at cell boundaries. The average diameter of dislocation cells in the as-built condition was around ~0.6 μm (Table 2). As presented in our previous study [15], high thermal gradients and rapid cooling during the solidification process of LPBF generated fine solidification cells with dense dislocation tangles at boundaries. These solidification cells are well preserved after the cyclic loading at room temperature (Figure 5 b-e). Although the cell dimensions did not change, the dislocation network at cell boundaries appeared more organised after cyclic loading at 22 °C (Figure 5 b). Increasing the loading temperature resulted in less organised cells in comparison to those after fatigue at and 200 °C (Figure 5 c-e). In particular, the dislocation networks at 400 °C and 600 °C were seen to be partially destroyed (Figure 5 d,e). Such destruction is exhibited by the observation of untangled dislocations after fatigue at elevated temperatures (Figure 5 d,e). The reduction in dislocation density is more notable at 600 °C that individual dislocations at cell boundaries can be distinguished compared to the samples tested at lower temperatures. Effect of the test temperature is also observed on the cell structure and diameter. The dislocation cell walls became thicker, but less dense; and the average dislocation cell diameter increased from 0.60 μm to 0.68 μm when the fatigue test temperature increased from 22 °C to 400 °C (Table 2). Cells at 600 °C appeared to be slightly smaller (0.63 μm) than that at 400; however, they were very ill organized with thin cell walls – so the comparison of the size was not really applicable. In addition, recrystallisation was not observed after cyclic loading at 600 °C. This observation is in good agreement with previous studies showing that the solidification microstructure was stable after the compression test at 600 °C [44,78], when partial recrystallisation was only seen at 700 °C [44], and the solidification microstructure was seen to disappear at 900 °C [78]. At a given loading temperature, the change in strain rate did not result in considerable variation in the cell microstructure.

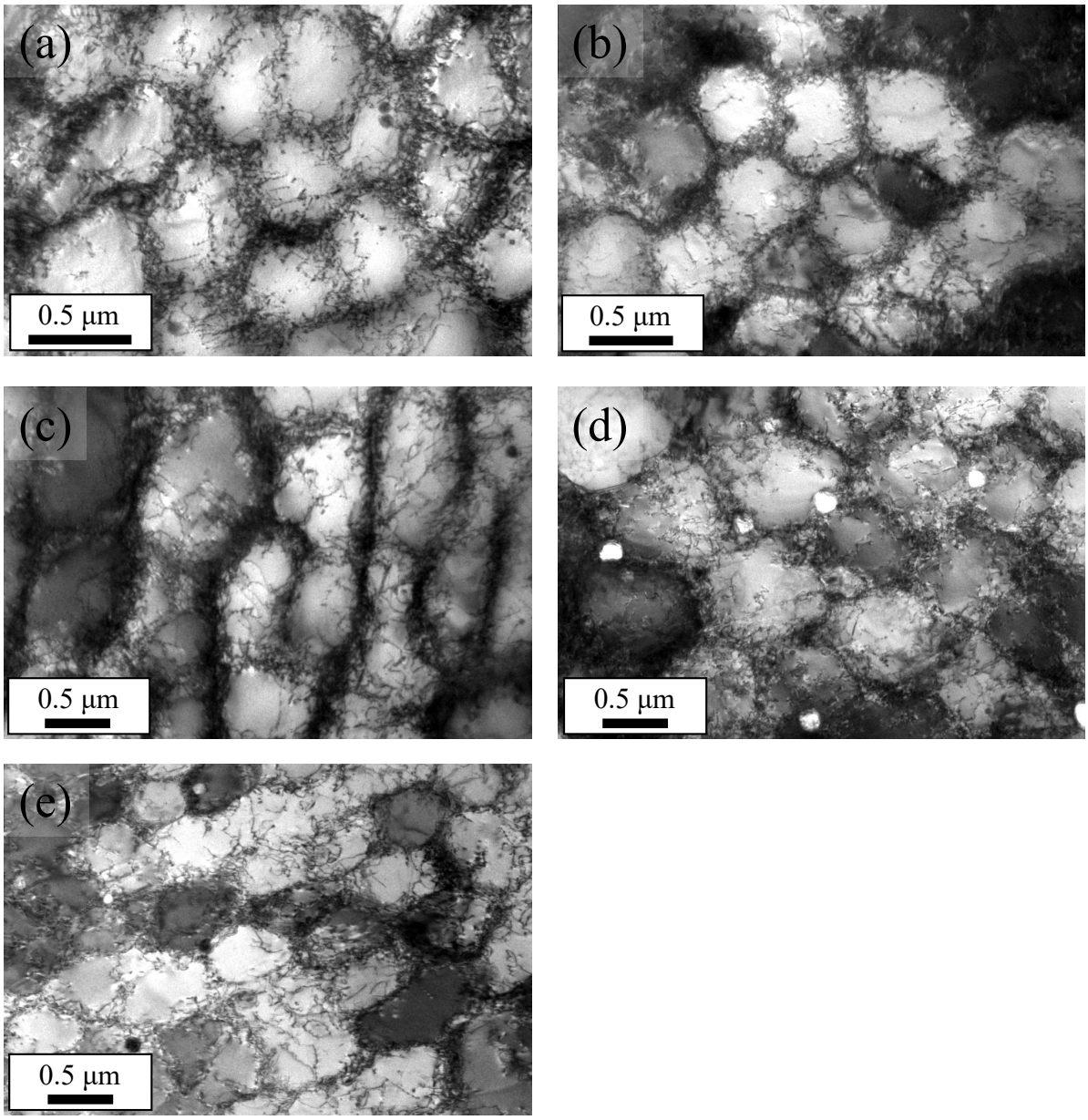


Figure 5. Celllular microstructure in the LPBF CrMnFeCoNi HEA: (a) in as-built condition, and after cyclic loading at the strain rate of 10^{-3} 1/s at (b) 22 °C, (c) 200 °C, (d) 400 °C and (e) 600 °C. Note that particles with the bright contrast (most visible in (d) were also present at the other studied temperatures and were identified to be manganese oxides [15].

3.4 Thermally activated dependence of yield stress, friction and back stresses

Figure 6 shows the evolution of the measured yield stress at an offset strain of 0.01 % during cyclic loading for the different temperatures and strain rates. This result shows the temperature dependence of yield stresses; whereby the higher the temperature the lower the yield stress. The largest reduction of the yield stress occurred when temperature increased to 200 °C from 22 °C, while the magnitudes of reduction when the temperature increased further from 200 °C to 400 °C and from 400 °C to 600 °C was similar and lower. The yield stress at the higher strain (10^{-2} s^{-1}) was larger than that of the lower strain (10^{-3} s^{-1}) for every cycle at 22 °C, exhibiting a positive strain rate sensitivity. The samples tested at 22 °C exhibited a short cyclic hardening behaviour during the first 10 cycles with a small increase in the yield stress regardless of strain rates. The increase of the yield stress due to the cyclic hardening was negligible but still noticeable during the first 2~3 cycles of loading at 200 °C but became unnoticeable as the temperature increased over 400 °C. Regarding strain rate dependence, the yield stresses at 200 °C for both the strain rates were similar throughout the cyclic softening stage until the ~500th cycle. However, they became different after the 500th cycle with the yield stress at 10^{-2} s^{-1} being smaller than that of the 10^{-3} s^{-1}, showing a possible negative strain rate sensitivity. This negative strain rate sensitivity was more obvious and started at an earlier cycle at 400 °C. In particular, the yield stress from about the 200th cycle at 10^{-3} s^{-1} became clearly higher than that at the higher strain rates thanks to a noticeable secondary cyclic hardening at the 10^{-3} s^{-1}, confirming the negative strain rate sensitivity. At 600 °C, the fatigue life was very short and there was no significant difference in yield stress between the two strain rates.

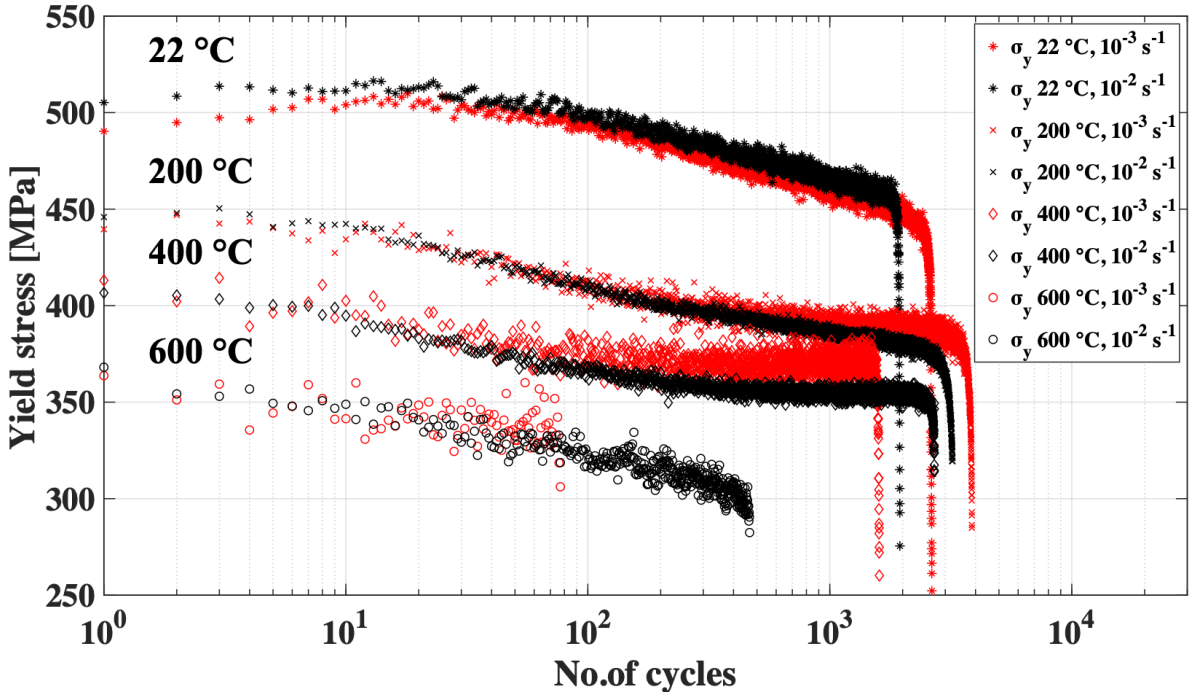


Figure 6. Evolution of the yield stress at an offset strain of 0.01 % after cyclic loading at 22-600 °C and strain rates of 10^{-3} s^{-1} (red symbols) and 10^{-2} s^{-1} (black symbols)

Friction stress and back stress were calculated to assist in relating the cyclic deformation to the microstructural evolution during cyclic loading according to Cottrell [60,72]. The evolution of friction stress and back stress during cyclic loading is shown in Figure 7. While friction stress exhibited a similar dependence on thermally activated factors (such as temperature and strain rate) as that of the yield stress (Figure 7a versus Figure 6), the back stress (Figure 7b) showed a much less dependence on temperature and strain rate. This is in consistence with the characteristic nature of the long-range interaction of dislocations of back stress, increasing the insensitivity of back stress to the thermal assistance [59,79]. However, the back stress still decreased when temperature increased (Figure 7b) in particular in the first 100 cycles of cyclic deformation. The variation in back stress was increasingly diminished when the temperature increased to be above 200 °C for the two strain rates. Towards the end of the cyclic softening, the back stress converged to almost the same level for all strain rates and temperatures (Figure 7b).

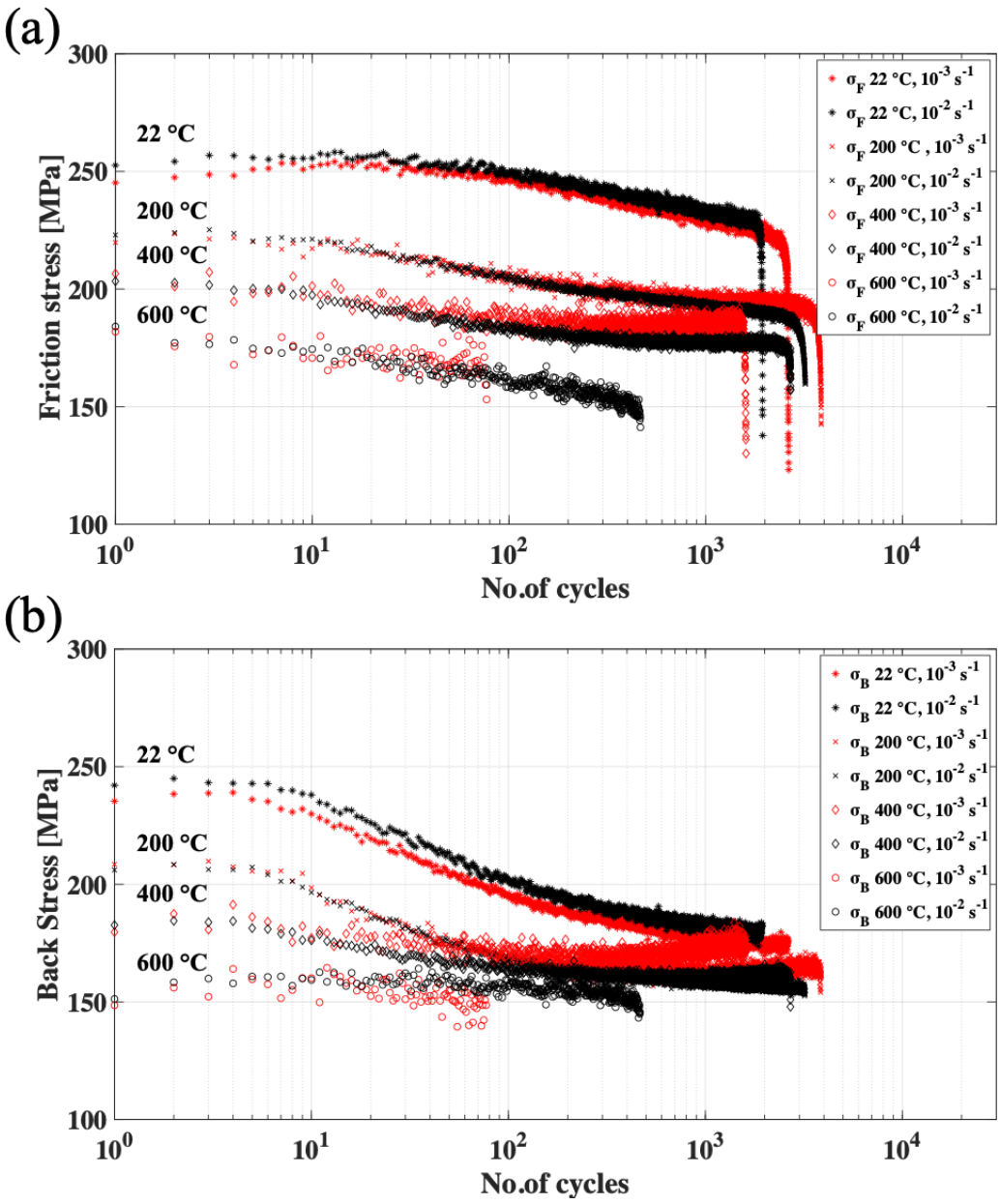


Figure 7. Thermally activated dependence of friction and back stresses during the tension-going loading at the four different temperatures 22, 200, 400 and 600 °C and two strain rates of 10^{-3} s^{-1} (red symbols) and 10^{-2} s^{-1} (black symbols): (a) friction stresses, (b) back stresses.

3.3 The similitude relation

The similitude relationship states that dislocation cells with a given size develop from dislocation forests in response to an applied stress of cyclic plastic loading and the strength of crystalline alloys is inversely proportional to the size of the formed dislocation cells [61,62,64–66]. Assuming that there were no dislocation cells before the cyclic deformation, this section estimates the size of dislocation cells that should form in response to the applied cyclic load. Hence, the similitude relationship (i.e., Equation 3) was used to calculate the cell size required in response to applied stresses should no dislocation cells be present before cyclic loading (Table 2). The calculated size was subsequently compared to the average of the dislocation cell diameters experimentally measured before and after fatigue at the different temperatures to discuss the stability of as-built cells in thermal fatigue. With the typical range of K for FCC metals (from 5 to 10) [64], Table 4 shows that the measured cell sizes are lying in between the calculated ones. To get the best fit against the measured sizes, the value of K should be varied between $7.77 - 8.28 \pm 0.3$. There is a slight variation in the calculated K for the four different temperatures, but the variation appears insignificant.

Table 4. The measured average dislocation cell diameters after fatigue, calculated cell diameters with assumed similitude coefficients and calculated similitude coefficient based on the measured cell diameter

Temperature (°C)	Measured average cell diameter after fatigue (μm)	Calculated cell diameter (μm) with $K = 5$	Calculated cell diameter (μm) with $K = 10$
22	0.60	0.38 ± 0.03	0.76 ± 0.05
200	0.65	0.42 ± 0.03	0.83 ± 0.05
400	0.68	0.41 ± 0.03	0.82 ± 0.05
600	0.63	0.38 ± 0.03	0.77 ± 0.05

3.6 Evolution of the loop shape parameter and strain energy density

The hysteresis loop change, characterised by a shape parameter, during cyclic loading reflects the evolution of microstructure and internal stresses [40]. The shape of the hysteresis loop remains slim and pointed during cyclic hardening loading, resulting in a decrease in the loop shape parameter during the cyclic hardening stage. On the other hand, hysteresis loop became more rectangular, resulting in an increase in the loop shape parameter as explained in previous studies on 316L [57,71]. Consistent with these trends, Figure 8a shows that the loop shape parameter at 22 °C for the two strain rates did decrease in the first ~5 cycles of the cyclic hardening, then the loop shape parameter increased gradually until the end of fatigue life due to the cyclic softening. This trend is also observed when samples were tested at 200 °C and 400 °C, as shown in Figure 8c and Figure 8e, respectively. Table 3 showed the absolute rate of softening decreased when the temperature was increased. Hence, Figure 8 shows the rising gradients of loop shape parameter curves at 200 °C and 400 °C are less steep than that at 22 °C, whereas the loop shape parameter curves at 600 °C remain almost constant throughout cyclic loading. As aforementioned, a secondary hardening was observed at 400 °C and 10^{-3} s^{-1} (Figure 8e). Correspondingly, after the primary decrease then increase, the loop shape parameter curve for the condition of 400 °C and 10^{-3} s^{-1} decreased again from the ~500^{th} cycle due to the secondary cyclic hardening (Figure 8e). Interestingly, although the secondary hardening was not clearly seen in other test conditions in Figure 6, Figure 8c and e show decreases of the loop shape parameter at 200 °C and 10^{-3} s^{-1} (from the ~2000^{th} cycle) and at 400 °C and 10^{-2} s^{-1} (from the ~1500^{th} cycle), suggesting that the secondary hardening would also occur for the two test conditions.

The right column of Figure 8 (b, d, f and h) is the evolution of strain energy density per cycle at the temperature range of 22-600 °C. In general, the strain energy density during cyclic loading decreased as the test temperature increased; energy per cycle was highest at 22 °C then gradually decreased at elevated temperatures. The strain energy density per cycle at room temperature slightly decreased in the cyclic hardening, subsequently increased during cyclic softening from about 320 J/m^3 to about 340 J/m^3 during the first 200 cycles, then became saturated until the end of cyclic loading. The same trend was seen for 200 °C and 400 °C, but with lower rates of change: At 200 °C, the energy per cycle was about 305-310 J/m^3 at the early stage of cyclic loading then increased during the first 100 cycles, then saturated at about 310-315 J/m^3. At 400 °C, energy per cycle was about 285-290 J/m^3, but only insignificantly increased to 295 J/m^3 for the lower strain rate (10^{-3} s^{-1}) or remained almost unchanged for the higher strain rate (10^{-2} s^{-1}). For all the temperatures, the strain energy density per cycle at the two strain rates was almost the same.

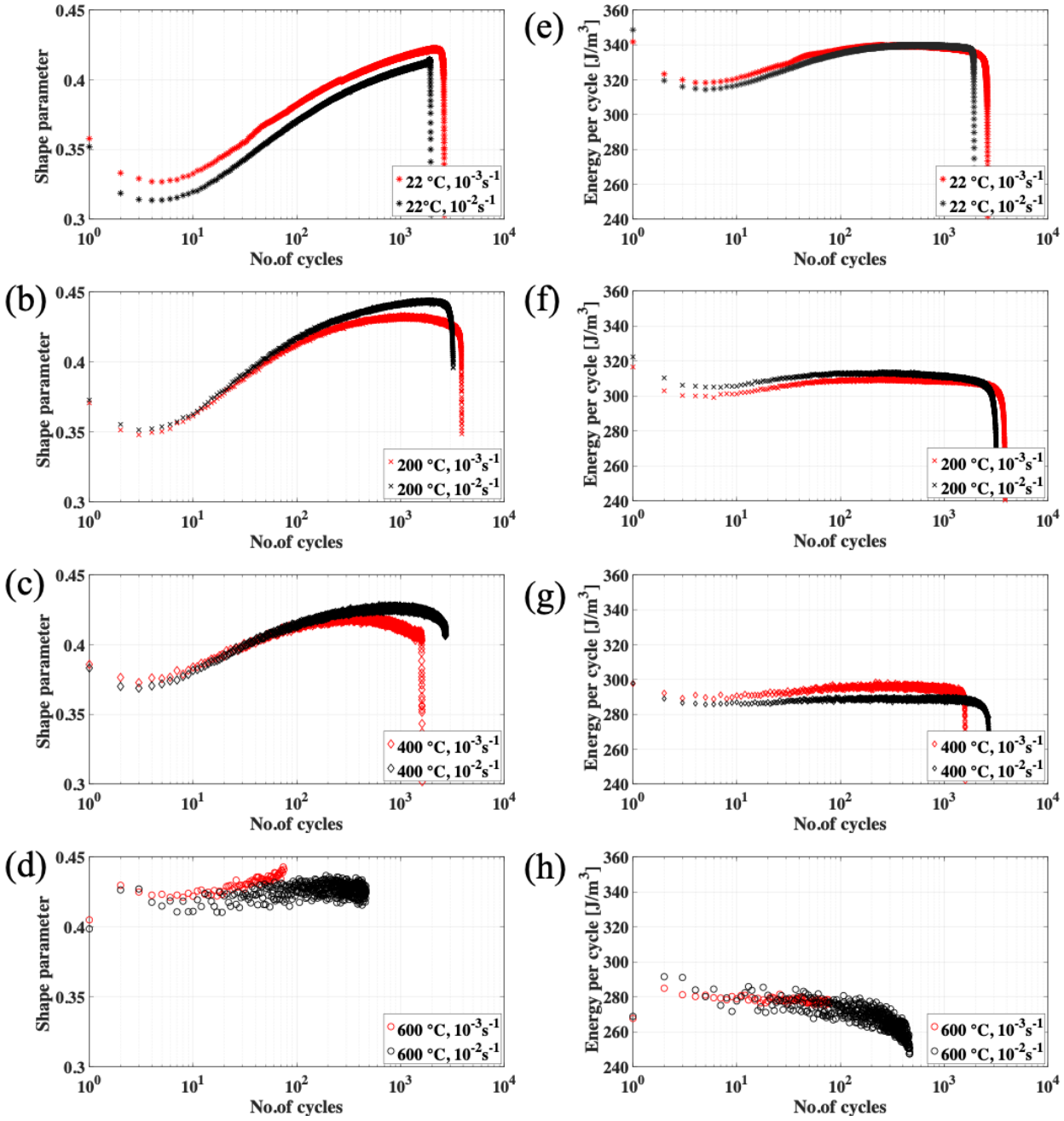


Figure 8. The left column is the evolution of hysteresis loop shape parameter of the CrMnFeCoNi HEA samples during cyclic loading at (a) 22 °C, (c) 200 °C, (e) 400 °C and (g) 600 °C. The right column is the evolution of strain energy of the CrMnFeCoNi HEA samples during cyclic loading at (b) 22 °C, (d) 200 °C, (f) 400 °C and (h) 600 °C

3.7 Fractography

Fracture surfaces of all fatigued samples tested at 22, 200 and 400 °C are seen to be transgranular with fatigue striations (Figure 9a-c). Large lack of fusion defects were observed in the fracture surface of the samples tested at 22 °C and 400 °C. These defects were likely the initiation site of dominant cracks, as highlighted in our previous study [15]. In contrast, the fracture surface of the sample tested at 600 °C shows more intergranular characteristic. This transition from transgranular to intergranular fracture at 600 °C corresponds to a significant reduction in the fatigue life at 600 °C in comparison to the other temperatures (Table 3).

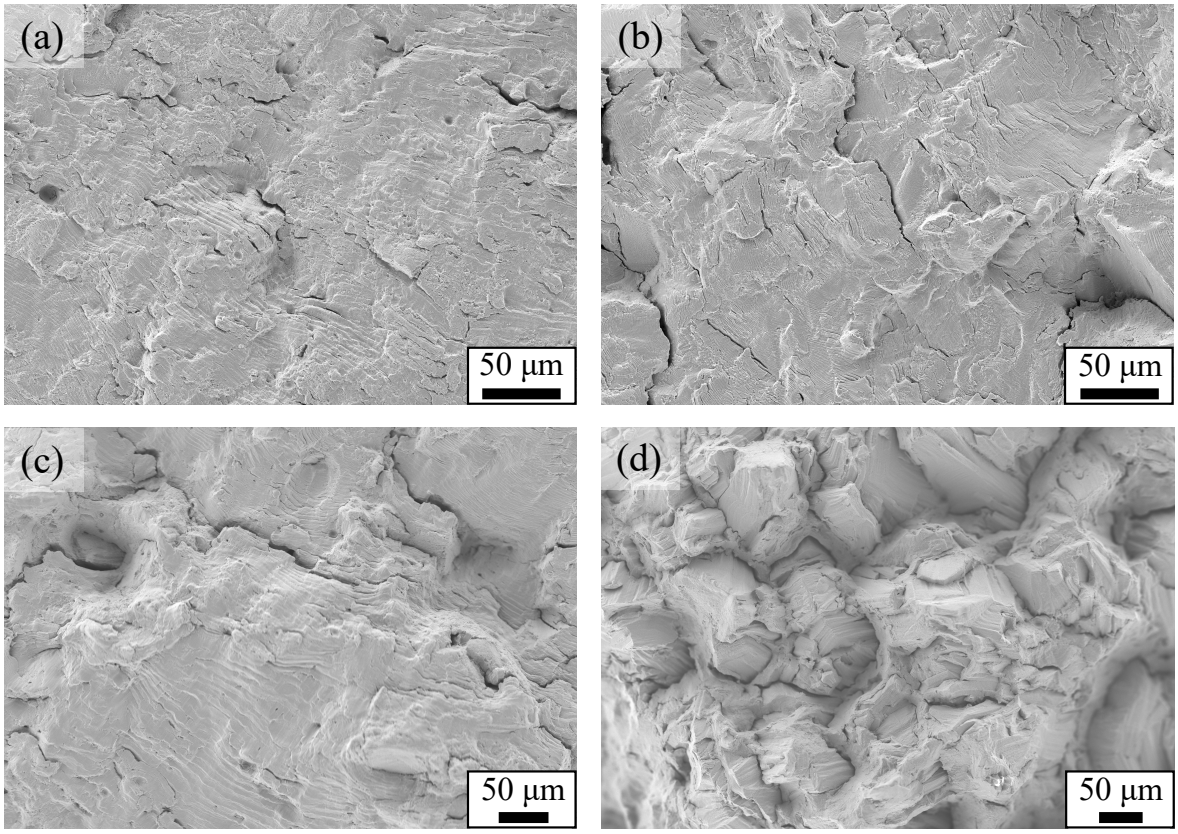


Figure 9. SEM fractography of the samples tested at 22-600 °C and strain rate 10^{-2} s^{-1}. (a) 22 °C, (b) 200 °C, (c) 400 °C, and (d) 600 °C

Figure 10a shows a pattern of domains on the fracture of the sample tested at 600 °C at a higher magnification. The seen pattern contains features resembling the helical grain microstructure observed for the HEA fabricated by the chessboard with 67° rotation between layers (Figure 10c and d). The helical grain microstructure is due to the in-layer and out-of-layer side-branching promoted in the chessboard pattern as explained in detail in [11]. Similarly, the domains on fracture surface were aligned in average of about 63° to the others (Figure 10b), which is close to the rotation angle of 67°. Furthermore, the size of the domain shown in Figure 10a ranged from 70 µm to 100 µm which is comparable to the grain size observed on the EBSD maps (Figure 10c and d). This observation indicates that the grain microstructure strongly governed the fatigue crack propagation and provides additional support that the fracture at 600 °C was probably intergranular.

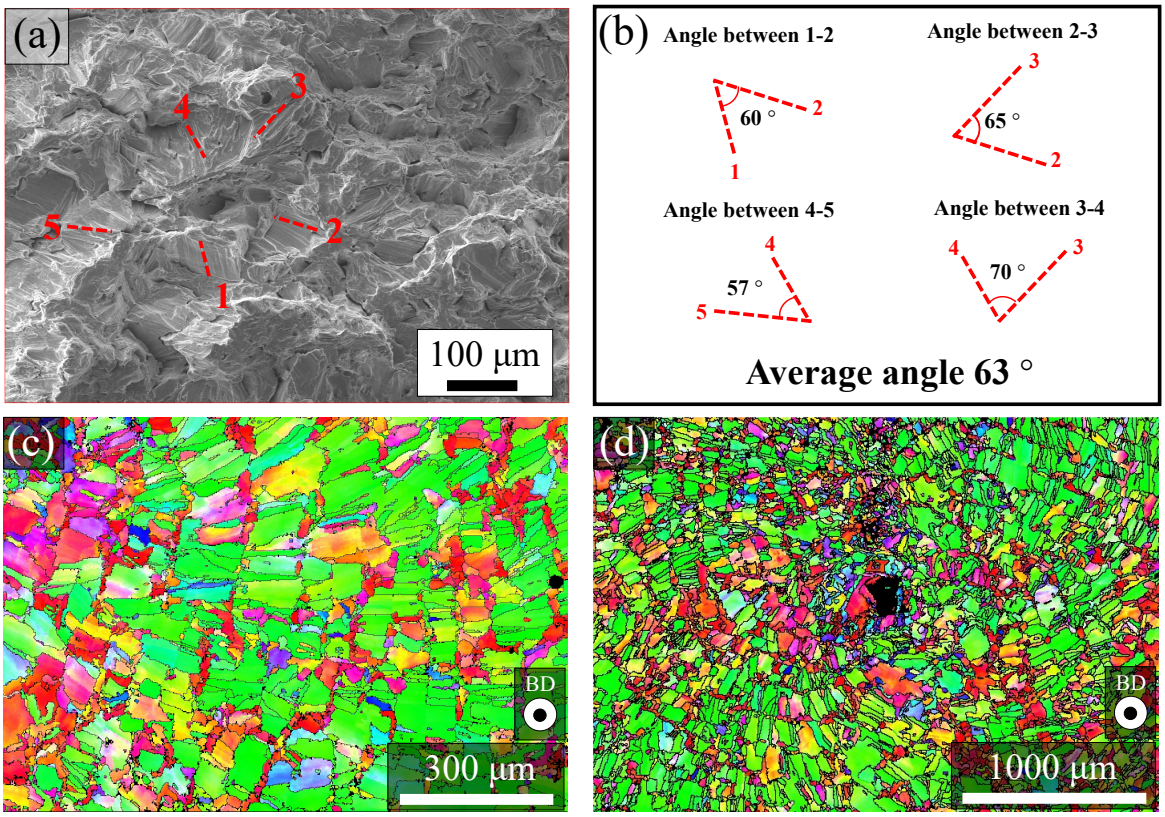


Figure 10. Fractography of fatigued sample tested at 600 °C and strain rate 10^{-2} s^{-1}. (a) Domains aligned in a pattern resembling to the helical grain microstructure observed in the HEA fabricated by the chessboard with 67° rotation between layers. Red dash lines were drawn to measure the angles between domains. (b) The measured angles between each domain and with an average anlge of 63 °. (c) Grain microstructure shown in IPF-Z map of as-built build fabricated by a chessboard scan (BD: out of page, and Z-axis is parallel to BD), (d) IPF-Z image of a region in (c) at a lower magnification showing a pattern similar to the pattern seen in (b).

4. Discussion

4.1 Cellular microstructure and cyclic deformation response

In a well-annealed FCC alloy (such as 316L stainless steel), the initial dislocation density is low without the presence of dislocation cells. The dislocation density significantly increases in the first cycles of loading to accommodate the prescribed strain. The increase in dislocations occurs most significantly near grain boundaries because of plastic incompatibility between grains due to grain misorientations [53,57,59]. The increase of dislocation density results in more interactions (including self and cross-slip interactions) between dislocations, causing the primary cyclic hardening. Upon further cyclic loading, dislocations start annihilating and rearranging to a structure of a low energy such as dislocation cellular structure [53,57,59]. Hereafter, such dislocation cellular structure induced by the mechanical cyclic loading is named fatigue dislocation cells. In contrast to the annealed condition, the as-built condition of an alloy fabricated by LPBF already contains the solidification cellular (or dendritic) microstructure consisting of dense dislocation at the cell boundaries (Figure 5), making solidification microstructure very similar to the dislocation cellular structure formed in fatigue. The as-built dislocations cells in LPBF HEA are generated as the high thermal gradient in melt-pools induces stress during solidification and subsequent cooling. Part of these as-built dislocations were necessary to accommodate the misorientation between solidification cells [10,15], but most of them were excessive. It should note that the as-built cells result from the fast solidification, and thermal stresses due to strong thermal gradient and thermal cycles in the repeated deposition. In other words, as-built cells share a lot of similarities with fatigue dislocation cells. The yield strength of as-built condition is found to be inversely proportional to the as-built cell size, implying that the as-built cells also follows the similitude law. Applying the similitude relationship Eqatuion. 1, 2 and 3 (with K = 7.5 – a typical value for FCC alloys [64]) to the as-built cells with the size of 0.60 μm (Section 3.3, Figure 5a), it estimated that the alloy could experience a equivalent thermal stress up to 787 MPa at 22 °C (673 MPa at 200 °C, 617 MPa at 400 °C, and 566 MPa at 600 °C) during the deposition. These estimated values of as-built stress are very similar the cyclic stress ranges (830 ± 30, 700 ± 30, 680 ± 20 and 620 ± 20 MPa at 22, 200, 400 and 600 °C, respectively) that were subsequently applied on the alloy after the fabrication. Therefore, the subsequently applied cyclic stress should result in similar dislocation cells (Table 4), i.e. there was no drive force for further evolution of the as-built cells. In addition, the dense immobile dislocation junctions and chemical segegration at the as-built cell boundaries [15] stabilise the finer, as-built cells [7]. Consequently, as-built cells should be stable upon the subsequent cyclic loading. This explains why the cells remained unchanged after fatigue in particular at 22 °C (Figure 5 b vs a). However, the dislocation mobility increases thanks to the thermal assistance at higher temperatures promotes the dynamic recovery and the unzipping of dislocation junctions [80] at the cell boundaries, and reduces the pinning effects of chemical segregated elements. Thereby, the increased mobility facilitates the untanglement of as-built dislocation cellular structure, explaining why there were coarsening and untanglement of the cells in cyclic loading at the elevated temperatures (Figure 5c-e) and Table 4.

The high density of dislocations already present in the as-built state means a smaller number of mobile dislocations needs to be generated in order to accommodate the prescribed strain. Hence, the number of cycles required to generate dislocations was short and softening started soon. This is indeed seen in the cyclic deformation behaviour of the LPBF HEA. The cyclic hardening behaviour (Figure 3a and Figure 6) was much shorter (with a low hardening rate) in comparison to that of the annealed CrMnFeCoNi and other FCC alloys such as 316L that often have longer cyclic hardening with significantly higher hardening rates [42,58,59]. Figure 7 shows that the increase in dislocation density

during the cyclic hardening induced an increase in friction stress, but not back stress because the friction stress depends on short-range interactions of dislocations while the back stress is mainly dependent on the long-range interactions of collective dislocations. The movement of dislocations also promotes the annihilation of dislocations. The annihilation rate increases with increasing the dislocation density, i.e. dynamic recovery [81]. Once the dislocation density reaches a peak of the cyclic hardening, the annihilation of dislocations outweighs the generation, causing the decrease in the dislocation density. Furthermore, dislocations start to rearrange to form a lower energetic configuration such as dislocation dipoles in the cell boundaries with clearer cell interiors, allowing a lower density of mobile dislocations to accommodate the same prescribed strain. The decrease in dislocation density and rearrangement of dislocations result in the cyclic softening. While the friction stresses reduced with a low rate cyclic softening (Figure 7a), the annihilation and rearrangement of dislocations resulted in lower energy configurations which led to a significantly greater decrease in back stress during the softening stage (Figure 7b), causing the back stress to dominate the cyclic softening deformation response in the LPBF HEAs.

4.2 Effect of temperature and strain rate and dynamic strain ageing on fatigue behaviour

Dislocations are often more mobile with increasing temperature as a consequence of thermal assistance. The prescribed strain can be accommodated by a smaller number of dislocations with higher mobility. High mobility, in turn, enables dislocations to find lower energetic configurations more quickly compared to at lower temperatures. Thus, a shorter cyclic hardening (Figures 5 and 6) and a relatively smaller number of necessary dislocations required to accommodate the plastic deformation at elevated temperatures. Indeed, the GND density in the region close to the fracture surface (e.g. within 75 μm from the fracture surface) at elevated temperatures, especially at 400 °C and 600 °C (Figure 4d and e), was lower than at 22 °C and 200 °C (Figure 4b and c). As mentioned in previous section 4.1, dislocations rearrange themselves into lower energetic configurations at cell boundaries during cyclic loading, and accordingly, the formation of more compact dislocation networks is shown in the samples tested at lower temperatures (22 °C and 200 °C, Figure 5b and c, respectively). However, the increased mobility of dislocations at elevated temperatures also caused more frequent annihilation of dislocations and unzipping of dislocation junctions, resulting in the annihilation of dislocations outweighing the generation of dislocations. The annihilation and rearrangement of dislocations occur earlier and faster at elevated temperatures, causing a shorter cyclic softening phase (Figure 5 and 6). The decrease in dislocation density is responsible for reducing the strain energy of the CrMnFeCoNi HEA samples at elevated temperatures (Figure 8). Furthermore, the dislocation networks at cell boundaries are seen to be increasingly untangled after the cyclic loading with increasing temperature, explaining the increasingly less organised dislocation cells after fatigue with increasing the temperature in Figure 5. Thus, the dislocation cell walls became thicker, and the cell diameter increased as the dislocation mobility increased and dislocation networks lost their compactness at elevated temperatures (Table 4). Furthermore, the long-range stress field in the LPBF HEA tested at elevated temperatures is weaker than that of the lower temperatures as the shear modulus decreases with temperature (Table 2) and dislocation networks were less well organised, causing the decrease in back stress with temperature (Figure 7b). However, the back stress curves stabilised and reached a similar value for the temperatures from 200°C to 600°C, indicating the long-range stress field after the large number of cycles at these temperatures was quite similar.

In general, the difference in apparent yield stress, friction stress, back stress, loop shape parameter values and energy per cycle between the two different strain rates over the tested temperature range is noticeable but insignificant, suggesting the strain rate dependence of LPBF HEAs in this range of strain rate is low. The LPBF HEAs at room temperature (22 °C) exhibits positive strain rate

sensitivity. In other words, the apparent yield stress, friction stress and back stress values at the higher strain rate (10^{-2} s^{-1}) are larger than those at the lower strain rate (10^{-3} s^{-1}) (Figure 6 and Figure 7). Also, the hysteresis loop shape parameter values at the higher strain rate are lower than that of the lower strain rate (Figure 8). The positive strain rate sensitivity is due to the higher stress required for dislocations to overcome a larger drag force to accommodate the same plastic deformation at a higher strain rate. However, the rate sensitivity was gradually reversed with the temperature in the range of 200°C to 400°C. The presence of both secondary hardening at 400 °C and negative strain sensitivity indicates dynamic strain ageing (Figure 6). Dynamic strain ageing (DSA) occurs due to the short-range interaction between dislocations and solute atoms over a certain range of temperatures and strain rates [82]. Because solute atoms are more active with increasing temperature, more solute atoms diffuse into dislocation cores and form an atmosphere of solute atoms. Such atmospheres can arrest dislocations. Once arrested, a higher stress is required to unlock the dislocations and accommodate plastic deformation. At the critical stress, the dislocations can overcome the pinning and start to glide, causing a stress drop until the next interaction with solute atoms. The observation of DSA in this study is in agreement with other studies of CrMnFeCoNi and its derivatives [83–85]. In addition, Carroll *et al.* and Wu *et al.* observed serrations due to dynamic strain ageing at high temperatures in the alloys (CoFeNi, CoCrFeNi, NiCoCr, FeNiMn, NiCoMn, FeNiCoMn and NiCoCrMn) which are compositional subsets of the CrMnFeCoNi [84,85]. Therefore, it is difficult to specify the elements responsible for dynamic strain ageing. Nevertheless, the lowest activation energy for diffusion of manganese amongst five principle elements [86] suggest manganese would be one of the responsible elements for dynamic strain ageing. Stress serration is not the single characteristic of DSA. Even without the evidence of stress serration, DSA might still be active and exhibited via another characteristic that is the negative strain rate sensitivity [87,88]. The mobility of dislocations is lower with decreasing the strain rate, allowing solute atoms to form an atmosphere around dislocation cores, requiring a higher stress to move dislocations. If the strain rate is increased, the slip rate of dislocation is higher, making the formation of solute atom atmospheres (hence DSA) more difficult. Therefore, the flow stress is higher at lower strain rate, i.e., the negative strain rate sensitivity. Even if DSA was not noticeably active in the early deformation, it was found that DSA could happen after a certain number of cycles during cyclic loading once vacancies accumulated sufficiently to assist the diffusion of solute atoms [82]. Such an occurrence of DSA later in fatigue life caused a negative strain rate sensitivity and a secondary cyclic hardening [82]. Figure 6 and Figure 7 confirm a negative strain rate sensitivity and the secondary cyclic hardening, in particular after about 200 cycles at 400 °C and 10^{-3} s^{-1}, providing evidence of the presence of DSA. The strong interactions between dislocations and solute atoms at those strain rate and temperature was sufficient to pin dislocations and subsequently cause secondary cyclic hardening behaviour after a certain number of cycles. Therefore, the secondary cyclic hardening observed in this study is attributed to the DSA occurrence later in fatigue life. The loop shape parameter reflects the evolution of microstructure and cyclic deformation response during fatigue. A decrease in the loop shape is associated with an increase in dislocation density and cyclic hardening, while an increase of the loop shape parameter is due to dislocation rearrangement and cyclic softening [57]. A secondary decrease of the loop shape parameter well before substantial drop due to the fatigue damage was seen for the strain rate of 10^{-3} s^{-1} at 200 °C and 400 °C and (Figure 8c and e). This secondary decrease is due to higher numbers of dislocations required to accommodate the same plastic strain because DSA happened. Secondary cyclic hardening was not seen despite the DSA was observed at 200 °C. The diffusion rate of solute atoms at 200 °C was low and insufficient to cause secondary cyclic hardening behaviour. Furthermore, secondary cyclic hardening was not seen at 600 °C – this is because of 2 possible reasons: (1) the brittle intergranular-like fracture behaviour significantly lowered the fatigue life while it requires a certain number of cycles for DSA to occur, and (2) the mobility of solute atoms was high at this temperature, the solute atom atmosphere did not induce a pinning effect.

The mobility of point defects and solute atoms is comparatively higher at higher temperatures. Grain boundaries are known to be sinks for point defects and solute atoms, making them prone to crack initiation and preferential paths for propagation during cyclic loading at elevated temperatures. As consequently, the fracture mode of LPBF HEA changed from transgranular at 22-400 °C to more intergranular at 600 °C (Figure 9). This intergranular-like fracture behaviour resulted in more brittle failure and loss of ductility and significantly lowered the fatigue life at 600 °C regardless of strain rates.

5. Conclusion

The constitutive relationships between solidification microstructure and thermally-activated dependence of fatigue behaviour of the CrMnFeCoNi high-entropy alloy fabricated by laser powder-bed fusion have been discussed in this study. The presence of a high density of dislocations at cell boundaries enabled accommodation of the prescribed strain with a fewer number of dislocations required to be generated. Thus, a short period of cyclic hardening occurred with a low hardening rate in comparison to the annealed HEA. The cyclic softening deformation response is found to be governed by the back stress and showed less dependence on the friction stress. The annihilation and rearrangement of dislocations occur earlier and faster with a higher rate at elevated temperatures due to the thermal assistance. Thus, the dislocation networks at cell boundaries were increasingly destroyed and became less organised after fatigue with increasing temperature. As a consequence, the diameter and wall thickness of dislocation cells increased with the test temperature. The similitude relationship predicted that the thermal stress the alloy experienced in the fabrication was almost the same as the applied stress in the subsequent cyclic loading. Therefore, there was no driving force for further evolution of the fine as-built cells during the cyclic loading. Using the similitude relationship and an understanding of the chemical segregration, this study explains why the as-built fine cells should be stable in the cyclic loading. The decrease in dislocation density, and untanglement of cellular structure and the elastic modulus with increasing temperature were responsible for the decrease in cyclic strength, friction and back stress. There was an insignificant difference in cyclic stresses between the two strain rates used in this study (10^{-3} s^{-1} and 10^{-2} s^{-1}). However, the examination of strain rate dependence revealed the occurence of dynamic strain ageing (most noticeable at 400 °C) that caused the secondary cyclic hardening and negative strain rate sensitivity. The transition of fracture mode from transgranular at 22 °C to more intergranular-like at 600 °C resulted in more brittle failure and loss of ductility and significantly lowered the fatigue life at 600 °C.

Acknowledgements

We appreciate Dr. Paul. A. Hooper from the Department of Mechanical Engineering, Imperial College London for helping to manufacture the samples for fatigue tests. We acknowledge the financial support provided by the Excellent Funds for Frontier Research and the Imperial-Tsinghua Research and Innovation Seed Fund at Imperial College London.

6. References

[1] E. Yasa, J.P. Kruth, Microstructural investigation of selective laser melting 316L stainless steel parts exposed to laser re-melting, Procedia Eng. 19 (2011) 389–395. https://doi.org/10.1016/j.proeng.2011.11.130.

[2] A. Riemer, S. Leuders, M. Thöne, H.A. Richard, T. Tröster, T. Niendorf, On the fatigue crack growth behavior in 316L stainless steel manufactured by selective laser melting, Eng. Fract. Mech. 120 (2014) 15–25. https://doi.org/10.1016/j.engfracmech.2014.03.008.

[3] A.S. Wu, D.W. Brown, M. Kumar, G.F. Gallegos, W.E. King, An Experimental Investigation into Additive Manufacturing-Induced Residual Stresses in 316L Stainless Steel, Metall. Mater. Trans. A Phys. Metall. Mater. Sci. 45 (2014) 6260–6270. https://doi.org/10.1007/s11661-014-2549-x.

[4] K.N. Amato, S.M. Gaytan, L.E. Murr, E. Martinez, P.W. Shindo, Microstructures and mechanical behavior of Inconel 718 fabricated by selective laser melting, Acta Mater. 60 (2012) 2229–2239. https://doi.org/10.1016/j.actamat.2011.12.032.

[5] L.L. Parimi, G. Ravi, D. Clark, M.M. Attallah, Microstructural and texture development in direct laser fabricated IN718, Mater. Charact. 89 (2014) 102–111. https://doi.org/10.1016/j.matchar.2013.12.012.

[6] Q. Jia, D. Gu, Selective laser melting additive manufacturing of Inconel 718 superalloy parts: Densification, microstructure and properties, J. Alloys Compd. 585 (2014) 713–721. https://doi.org/10.1016/j.jallcom.2013.09.171.

[7] A. Piglione, B. Attard, V.V. Rielli, C.-T.S. Maldonado, M.M. Attallah, S. Primig, M.-S. Pham, On the constitutive relationship between solidification cells and the fatigue behaviour of IN718 fabricated by laser powder bed fusion, Addit. Manuf. 47 (2021) 102347. https://doi.org/10.1016/j.addma.2021.102347.

[8] L.E. Murr, S.M. Gaytan, F. Medina, E. Martinez, J.L. Martinez, D.H. Hernandez, B.I. Machado, D.A. Ramirez, R.B. Wicker, Characterization of Ti-6Al-4V open cellular foams fabricated by additive manufacturing using electron beam melting, Mater. Sci. Eng. A. 527 (2010) 1861–1868. https://doi.org/10.1016/j.msea.2009.11.015.

[9] J. Lertthanasarn, C. Liu, M.S. Pham, Synergistic effects of crystalline microstructure, architected mesostructure, and processing defects on the mechanical behaviour of Ti6Al4V meta-crystals, Mater. Sci. Eng. A. 818 (2021) 141436. https://doi.org/10.1016/j.msea.2021.141436.

[10] M.S. Pham, B. Dovgyy, P.A. Hooper, Twinning induced plasticity in austenitic stainless steel 316L made by additive manufacturing, Mater. Sci. Eng. A. 704 (2017) 102–111. https://doi.org/10.1016/j.msea.2017.07.082.

[11] M.S. Pham, B. Dovgyy, P.A. Hooper, C.M. Gourlay, A. Piglione, The role of side-branching in microstructure development in laser powder-bed fusion, Nat. Commun. 11 (2020) 1–12. https://doi.org/10.1038/s41467-020-14453-3.

[12] Z. Qiu, C. Yao, K. Feng, Z. Li, P.K. Chu, Cryogenic deformation mechanism of CrMnFeCoNi high-entropy alloy fabricated by laser additive manufacturing process, Int. J. Light. Mater. Manuf. 1 (2018) 33–39. https://doi.org/10.1016/j.ijlmm.2018.02.001.

[13] R. Li, P. Niu, T. Yuan, P. Cao, C. Chen, K. Zhou, Selective laser melting of an equiatomic CoCrFeMnNi high-entropy alloy: Processability, non-equilibrium microstructure and mechanical property, J. Alloys Compd. 746 (2018) 125–134. https://doi.org/10.1016/j.jallcom.2018.02.298.

[14] A. Piglione, B. Dovgyy, C. Liu, C.M. Gourlay, P.A. Hooper, M.S. Pham, Printability and microstructure of the CoCrFeMnNi high-entropy alloy fabricated by laser powder bed fusion, Mater. Lett. 224 (2018) 22–25. https://doi.org/10.1016/j.matlet.2018.04.052.

[15] M. Jin, A. Piglione, B. Dovgyy, E. Hosseini, P.A. Hooper, S.R. Holdsworth, M.-S. Pham, Cyclic plasticity and fatigue damage of CrMnFeCoNi high entropy alloy fabricated by laser powder-bed fusion, Addit. Manuf. 36 (2020) 101584. https://doi.org/10.1016/j.addma.2020.101584.

[16] T. Mukherjee, J.S. Zuback, A. De, T. DebRoy, Printability of alloys for additive manufacturing, Sci. Rep. 6 (2016) 1–8. https://doi.org/10.1038/srep19717.
[17] B. Cantor, I.T.H. Chang, P. Knight, A.J.B. Vincent, Microstructural development in equiatomic multicomponent alloys, 377 (2004) 213–218. https://doi.org/10.1016/j.msea.2003.10.257.
[18] B.J. Yeh, S. Chen, S. Lin, J. Gan, T. Chin, T. Shun, C. Tsau, Nanostructured High-Entropy Alloys with Multiple Principal Elements : Novel Alloy Design Concepts and Outcomes **, (2004) 299–303. https://doi.org/10.1002/adem.200300567.
[19] Y. Zhang, T. Ting, Z. Tang, M.C. Gao, K.A. Dahmen, P.K. Liaw, Z. Ping, Progress in Materials Science Microstructures and properties of high-entropy alloys, Prog. Mater. Sci. 61 (2014) 1–93. https://doi.org/10.1016/j.pmatsci.2013.10.001.
[20] M.H. Tsai, J.W. Yeh, High-entropy alloys: A critical review, Mater. Res. Lett. 2 (2014) 107–123. https://doi.org/10.1080/21663831.2014.912690.
[21] T. Fujieda, M. Chen, H. Shiratori, K. Kuwabara, K. Yamanaka, Y. Koizumi, A. Chiba, S. Watanabe, Mechanical and corrosion properties of CoCrFeNiTi-based high-entropy alloy additive manufactured using selective laser melting, Addit. Manuf. 25 (2019) 412–420. https://doi.org/10.1016/j.addma.2018.10.023.
[22] I. Kunce, M. Polanski, K. Karczewski, T. Plocinski, K.J. Kurzydlowski, Microstructural characterisation of high-entropy alloy AlCoCrFeNi fabricated by laser engineered net shaping, J. Alloys Compd. 648 (2015) 751–758. https://doi.org/10.1016/j.jallcom.2015.05.144.
[23] X. Yang, Y. Zhou, S. Xi, Z. Chen, P. Wei, C. He, T. Li, Y. Gao, H. Wu, Additively manufactured fine grained Ni6Cr4WFe9Ti high entropy alloys with high strength and ductility, Mater. Sci. Eng. A. 767 (2019) 138394. https://doi.org/10.1016/j.msea.2019.138394.
[24] M. Zhang, X. Zhou, D. Wang, W. Zhu, J. Li, Y.F. Zhao, AlCoCuFeNi high-entropy alloy with tailored microstructure and outstanding compressive properties fabricated via selective laser melting with heat treatment, Mater. Sci. Eng. A. 743 (2019) 773–784. https://doi.org/10.1016/j.msea.2018.11.118.
[25] P.K. Sarswat, S. Sarkar, A. Murali, W. Huang, W. Tan, M.L. Free, Additive manufactured new hybrid high entropy alloys derived from the AlCoFeNiSmTiVZr system, Appl. Surf. Sci. 476 (2019) 242–258. https://doi.org/10.1016/j.apsusc.2018.12.300.
[26] P.Y. Chen, C. Lee, S.Y. Wang, M. Seifi, J.J. Lewandowski, K.A. Dahmen, H.L. Jia, X. Xie, B.L. Chen, J.W. Yeh, C.W. Tsai, T. Yuan, P.K. Liaw, Fatigue behavior of high-entropy alloys: A review, Sci. China Technol. Sci. 61 (2018) 168–178. https://doi.org/10.1007/s11431-017-9137-4.
[27] M. Komarasamy, K. Alagarsamy, R.S. Mishra, Serration behavior and negative strain rate sensitivity of Al0.1CoCrFeNi high entropy alloy, Intermetallics. 84 (2017) 20–24. https://doi.org/10.1016/j.intermet.2016.12.016.
[28] H.Y. Yasuda, K. Shigeno, T. Nagase, Dynamic strain aging of Al0.3CoCrFeNi high entropy alloy single crystals, Scr. Mater. 108 (2015) 80–83. https://doi.org/10.1016/j.scriptamat.2015.06.022.
[29] Z. Tang, T. Yuan, C.W. Tsai, J.W. Yeh, C.D. Lundin, P.K. Liaw, Fatigue behavior of a wrought Al0.5CoCrCuFeNi two-phase high-entropy alloy, Acta Mater. 99 (2015) 247–258. https://doi.org/10.1016/j.actamat.2015.07.004.
[30] A. Gali, E.P. George, Tensile properties of high- and medium-entropy alloys, Intermetallics. 39 (2013) 74–78. https://doi.org/10.1016/j.intermet.2013.03.018.
[31] J.W. Bae, J. Moon, M.J. Jang, D. Yim, D. Kim, S. Lee, H.S. Kim, Trade-off between tensile property and formability by partial recrystallization of CrMnFeCoNi high-entropy alloy, Mater. Sci. Eng. A. 703 (2017) 324–330. https://doi.org/10.1016/j.msea.2017.07.079.
[32] M.J. Jang, S. Praveen, H.J. Sung, J.W. Bae, J. Moon, H.S. Kim, High-temperature tensile deformation behavior of hot rolled CrMnFeCoNi high-entropy alloy, J. Alloys Compd. 730 (2018) 242–248. https://doi.org/10.1016/j.jallcom.2017.09.293.
[33] B. Gludovatz, E.P. George, R.O. Ritchie, Processing, Microstructure and Mechanical Properties of the CrMnFeCoNi High-Entropy Alloy, Jom. 67 (2015) 2262–2270. https://doi.org/10.1007/s11837-015-1589-z.

[34] F. Otto, A. Dlouhý, C. Somsen, H. Bei, G. Eggeler, E.P. George, The influences of temperature and microstructure on the tensile properties of a CoCrFeMnNi high-entropy alloy, Acta Mater. 61 (2013) 5743–5755. https://doi.org/10.1016/j.actamat.2013.06.018.
[35] A. Amar, J. Li, S. Xiang, X. Liu, Y. Zhou, G. Le, X. Wang, F. Qu, S. Ma, W. Dong, Q. Li, Additive manufacturing of high-strength CrMnFeCoNi-based High Entropy Alloys with TiC addition, Intermetallics. 109 (2019) 162–166. https://doi.org/10.1016/j.intermet.2019.04.005.
[36] S. Xiang, J. Li, H. Luan, A. Amar, S. Lu, K. Li, L. Zhang, X. Liu, G. Le, X. Wang, F. Qu, W. Zhang, D. Wang, Q. Li, Effects of process parameters on microstructures and tensile properties of laser melting deposited CrMnFeCoNi high entropy alloys, Mater. Sci. Eng. A. 743 (2019) 412–417. https://doi.org/10.1016/j.msea.2018.11.110.
[37] B. Dovgyy, A. Piglione, P. Hooper, M.-S. Pham, Comprehensive assessment of the printability of CoNiCrFeMn in Laser Powder Bed Fusion, Mater. Des. 194 (2020) 108845. https://doi.org/10.1016/j.matdes.2020.108845.
[38] B. Gludovatz, A. Hohenwarter, D. Catoor, E.H. Chang, E.P. George, R.O. Ritchie, A fracture-resistant high-entropy alloy for cryogenic applications, Science (80-.). 345 (2014) 1153–1158. https://doi.org/10.1126/science.1254581.
[39] K.V.S. Thurston, B. Gludovatz, A. Hohenwarter, G. Laplanche, E.P. George, R.O. Ritchie, Effect of temperature on the fatigue-crack growth behavior of the high-entropy alloy CrMnFeCoNi, Intermetallics. 88 (2017) 65–72. https://doi.org/10.1016/j.intermet.2017.05.009.
[40] K.V.S. Thurston, B. Gludovatz, Q. Yu, G. Laplanche, E.P. George, R.O. Ritchie, Temperature and load-ratio dependent fatigue-crack growth in the CrMnFeCoNi high-entropy alloy, J. Alloys Compd. 794 (2019) 525–533. https://doi.org/10.1016/j.jallcom.2019.04.234.
[41] S.A.A. Shams, G. Jang, J.W. Won, J.W. Bae, H. Jin, H.S. Kim, C.S. Lee, Low-cycle fatigue properties of CoCrFeMnNi high-entropy alloy compared with its conventional counterparts, Mater. Sci. Eng. A. (2020) 139661. https://doi.org/10.1016/j.msea.2020.139661.
[42] K. Lu, A. Chauhan, D. Litvinov, M. Walter, A.S. Tirunilai, J. Freudenberger, A. Kauffmann, M. Heilmaier, J. Aktaa, High-temperature low cycle fatigue behavior of an equiatomic CoCrFeMnNi high-entropy alloy, Mater. Sci. Eng. A. 791 (2020) 139781. https://doi.org/10.1016/j.msea.2020.139781.
[43] D. Lin, L. Xu, H. Jing, Y. Han, L. Zhao, Y. Zhang, H. Li, A strong, ductile, high-entropy FeCoCrNi alloy with fine grains fabricated via additive manufacturing and a single cold deformation and annealing cycle, Addit. Manuf. 36 (2020) 101591. https://doi.org/10.1016/j.addma.2020.101591.
[44] Y.K. Kim, S. Yang, K.A. Lee, Superior Temperature-Dependent Mechanical Properties and Deformation Behavior of Equiatomic CoCrFeMnNi High-Entropy Alloy Additively Manufactured by Selective Laser Melting, Sci. Rep. 10 (2020) 1–13. https://doi.org/10.1038/s41598-020-65073-2.
[45] M.J. Jang, S.H. Joo, C.W. Tsai, J.W. Yeh, H.S. Kim, Compressive deformation behavior of CrMnFeCoNi high-entropy alloy, Met. Mater. Int. 22 (2016) 982–986. https://doi.org/10.1007/s12540-016-6304-2.
[46] S. Suresh, Fatigue of Materials, Cambridge University Press, 1998. https://doi.org/10.1017/CBO9780511806575.
[47] W. Schütz, A history of fatigue, Eng. Fract. Mech. 54 (1996) 263–300. https://doi.org/10.1016/0013-7944(95)00178-6.
[48] J. Schijve, Fatigue of structures and materials in the 20th century and the state of the art, Int. J. Fatigue. 25 (2003) 679–702. https://doi.org/10.1016/S0142-1123(03)00051-3.
[49] H. Mughrabi, Dislocation wall and cell structures and long-range internal stresses in deformed metal crystals, Acta Metall. 31 (1983) 1367–1379. https://doi.org/10.1016/0001-6160(83)90007-X.
[50] H. Mughrabi, Microstructural mechanisms of cyclic deformation, fatigue crack initiation and early crack growth, Philos. Trans. R. Soc. A Math. Phys. Eng. Sci. 373 (2015). https://doi.org/10.1098/rsta.2014.0132.
[51] D. Kuhlmann-Wilsdorf, C. Laird, Dislocation behavior in fatigue, Mater. Sci. Eng. 27 (1977) 137–156. https://doi.org/10.1016/0025-5416(77)90166-5.

[52] D. Kuhlmann-Wilsdorf, Theory of plastic deformation: - properties of low energy dislocation structures, Mater. Sci. Eng. A. 113 (1989) 1–41. https://doi.org/10.1016/0921-5093(89)90290-6.
[53] M.S. Pham, S.R. Holdsworth, Role of microstructural condition on fatigue damage development of AISI 316L at 20 and 300 °c, Int. J. Fatigue. 51 (2013) 36–48. https://doi.org/10.1016/j.ijfatigue.2013.02.005.
[54] Y.K. Kim, M.S. Baek, S. Yang, K.A. Lee, In-situ formed oxide enables extraordinary high-cycle fatigue resistance in additively manufactured CoCrFeMnNi high-entropy alloy, Addit. Manuf. 38 (2021) 101832. https://doi.org/10.1016/j.addma.2020.101832.
[55] F. Otto, C. Somsen, H. Bei, G. Eggeler, E.P. George, The influences of temperature and microstructure on the tensile properties of a CoCrFeMnNi high-entropy alloy, 61 (2013) 5743–5755. https://doi.org/10.1016/j.actamat.2013.06.018.
[56] G. Laplanche, A. Kostka, O.M. Horst, G. Eggeler, E.P. George, Microstructure evolution and critical stress for twinning in the CrMnFeCoNi high-entropy alloy, Acta Mater. 118 (2016) 152–163. https://doi.org/10.1016/j.actamat.2016.07.038.
[57] M.S. Pham, S.R. Holdsworth, Change of stress-strain hysteresis loop and its links with microstructural evolution in AISI 316L during cyclic loading, Procedia Eng. 10 (2011) 1069–1074. https://doi.org/10.1016/j.proeng.2011.04.176.
[58] M.S. Pham, S.R. Holdsworth, K.G.F. Janssens, E. Mazza, Cyclic deformation response of AISI 316L at room temperature: Mechanical behaviour, microstructural evolution, physically-based evolutionary constitutive modelling, Int. J. Plast. 47 (2013) 143–164. https://doi.org/10.1016/j.ijplas.2013.01.017.
[59] M.S. Pham, S.R. Holdsworth, Evolution of relationships between dislocation microstructures and internal stresses of AISI 316L during cyclic loading at 293 K and 573 K (20 °c and 300 °c), Metall. Mater. Trans. A Phys. Metall. Mater. Sci. 45 (2014) 738–751. https://doi.org/10.1007/s11661-013-1981-7.
[60] D. Kuhlmann-Wilsdorf, C. Laird, Dislocation behavior in fatigue II. Friction stress and back stress as inferred from an analysis of hysteresis loops, Mater. Sci. Eng. 37 (1979) 111–120. https://doi.org/10.1016/0025-5416(79)90074-0.
[61] M.R. Staker, D.L. Holt, The dislocation cell size and dislocation density in copper deformed at temperatures between 25 and 700°C, Acta Metall. 20 (1972) 569–579. https://doi.org/10.1016/0001-6160(72)90012-0.
[62] D. Kuhlmann-wilsdorf, A critical test on theories of work-hardening for the case of drawn iron wire, Metall. Trans. 1 (1970) 3173–3179. https://doi.org/10.1007/BF03038434.
[63] D. Kuhlmann-Wilsdorf, Theory of work hardening 1934-1984, Metall. Trans. A. 16 (1985) 2091–2108. https://doi.org/10.1007/BF02670414.
[64] M. Sauzay, L.P. Kubin, Scaling laws for dislocation microstructures in monotonic and cyclic deformation of fcc metals, Prog. Mater. Sci. 56 (2011) 725–784. https://doi.org/10.1016/j.pmatsci.2011.01.006.
[65] D. Kuhlmann-Wilsdorf, Theory of workhardening 1934-1984, Metall. Trans. A. 16 (1985) 2091–2108. https://doi.org/10.1007/BF02670414.
[66] H. Mecking, U.F. Kocks, C. Hartig, Taylor factors in materials with many deformation modes, Scr. Mater. 35 (1996) 465–471. https://doi.org/10.1016/1359-6462(96)00137-6.
[67] F. Bachmann, R. Hielscher, H. Schaeben, Texture analysis with MTEX- Free and open source software toolbox, Solid State Phenom. 160 (2010) 63–68. https://doi.org/10.4028/www.scientific.net/SSP.160.63.
[68] W. Pantleon, Resolving the geometrically necessary dislocation content by conventional electron backscattering diffraction, Scr. Mater. 58 (2008) 994–997. https://doi.org/10.1016/j.scriptamat.2008.01.050.
[69] H.J. Bunge, Some applications of the Taylor theory of polycrystal plasticity, Krist. Und Tech. 5 (1970) 145–175. https://doi.org/10.1002/crat.19700050112.
[70] C.A. Schneider, W.S. Rasband, K.W. Eliceiri, NIH Image to ImageJ: 25 years of image analysis, Nat. Methods. 9 (2012) 671–675. https://doi.org/10.1038/nmeth.2089.
[71] H. Mughrabi, The cyclic hardening and saturation behaviour of copper single crystals, Mater. Sci. Eng. 33 (1978) 207–223. https://doi.org/10.1016/0025-5416(78)90174-X.

[72] A. Cottrell, Dislocations and Plastic Flow in Crystals, Clarendon Press, Oxford, 1953.
[73] G.I. Taylor, The mechanism of plastic deformation of crystals. Part I.—Theoretical, Proc. R. Soc. London. Ser. A, Contain. Pap. a Math. Phys. Character. 145 (1934) 362–387. https://doi.org/10.1098/rspa.1934.0106.
[74] B. Gludovatz, E.P. George, R.O. Ritchie, Processing, Microstructure and Mechanical Properties of the CrMnFeCoNi High-Entropy Alloy, Jom. 67 (2015) 2262–2270. https://doi.org/10.1007/s11837-015-1589-z.
[75] L.R. Owen, E.J. Pickering, H.Y. Playford, H.J. Stone, M.G. Tucker, N.G. Jones, An assessment of the lattice strain in the CrMnFeCoNi high-entropy alloy, Acta Mater. 122 (2017) 11–18. https://doi.org/10.1016/j.actamat.2016.09.032.
[76] G. Laplanche, P. Gadaud, O. Horst, F. Otto, G. Eggeler, E.P. George, Temperature dependencies of the elastic moduli and thermal expansion coefficient of an equiatomic, single-phase CoCrFeMnNi high-entropy alloy, J. Alloys Compd. 623 (2015) 348–353. https://doi.org/10.1016/j.jallcom.2014.11.061.
[77] Y. Okada, Y. Tokumaru, Precise determination of lattice parameter and thermal expansion coefficient of silicon between 300 and 1500 K, J. Appl. Phys. 56 (1984) 314–320. https://doi.org/10.1063/1.333965.
[78] Z. Tong, X. Ren, J. Jiao, W. Zhou, Y. Ren, Y. Ye, E.A. Larson, J. Gu, Laser additive manufacturing of FeCrCoMnNi high-entropy alloy: Effect of heat treatment on microstructure, residual stress and mechanical property, J. Alloys Compd. 785 (2019) 1144–1159. https://doi.org/10.1016/j.jallcom.2019.01.213.
[79] U.. Kocks, A.S. Argon, M.F. Ashby, Thermodynamics and kinetics of slips, Prog. Mater. Sci. 19 (1975) 1–281. https://doi.org/10.1016/b978-0-408-01374-1.50020-8.
[80] B. Devincre, L.P. Kubin, Mesoscopic simulations of dislocations and plasticity, Mater. Sci. Eng. A. 234–236 (1997) 8–14. https://doi.org/10.1016/s0921-5093(97)00146-9.
[81] H. Mecking, U.F. Kocks, A Mechanism for Static and Dynamic Recovery, in: Strength Met. Alloy., Elsevier, 1979: pp. 345–350. https://doi.org/10.1016/B978-1-4832-8412-5.50063-1.
[82] M.S. Pham, S.R. Holdsworth, Dynamic strain ageing of AISI 316L during cyclic loading at 300°C: Mechanism, evolution, and its effects, Mater. Sci. Eng. A. 556 (2012) 122–133. https://doi.org/10.1016/j.msea.2012.06.067.
[83] K. Lu, A. Chauhan, D. Litvinov, M. Walter, A.S. Tirunilai, J. Freudenberger, A. Kauffmann, M. Heilmaier, J. Aktaa, High-temperature low cycle fatigue behavior of an equiatomic CoCrFeMnNi high-entropy alloy, Mater. Sci. Eng. A. 791 (2020) 139781. https://doi.org/10.1016/j.msea.2020.139781.
[84] Z. Wu, H. Bei, G.M. Pharr, E.P. George, Temperature dependence of the mechanical properties of equiatomic solid solution alloys with face-centered cubic crystal structures, Acta Mater. 81 (2014) 428–441. https://doi.org/10.1016/j.actamat.2014.08.026.
[85] R. Carroll, C. Lee, C.W. Tsai, J.W. Yeh, J. Antonaglia, B.A.W. Brinkman, M. Leblanc, X. Xie, S. Chen, P.K. Liaw, K.A. Dahmen, Experiments and Model for Serration Statistics in Low-Entropy, Medium-Entropy, and High-Entropy Alloys, Sci. Rep. 5 (2015) 1–12. https://doi.org/10.1038/srep16997.
[86] K.Y. Tsai, M.H. Tsai, J.W. Yeh, Sluggish diffusion in Co-Cr-Fe-Mn-Ni high-entropy alloys, Acta Mater. 61 (2013) 4887–4897. https://doi.org/10.1016/j.actamat.2013.04.058.
[87] A.W. Sleeswyk, Slow strain-hardening of ingot iron, Acta Metall. 6 (1958) 598–603. https://doi.org/10.1016/0001-6160(58)90101-9.
[88] R.C. Picu, A mechanism for the negative strain-rate sensitivity of dilute solid solutions, Acta Mater. 52 (2004) 3447–3458. https://doi.org/10.1016/j.actamat.2004.03.042.